IOP PUBLISHING PHYSICS IN MEDICINE AND BIOLOGY

Phys. Med. Biol. **52** (2007) 2775–2790 doi:10.1088/0031-9155/52/10/010

Resolution improvement in emission optical projection tomography

Johnathon R Walls[1], **John G Sled**[1], **James Sharpe**[2]
and R Mark Henkelman[1]

[1] Mouse Imaging Centre, Hospital for Sick Children, University of Toronto,
555 University Avenue, Toronto, ON M5G 1X8, Canada
[2] EMBL/CRG Systems Biology Unit, Centre for Genomic Regulation, Dr. Aiguader, 88,
08003 Barcelona, Spain

E-mail: johnathon.walls@utoronto.ca

Received 18 September 2006, in final form 8 March 2007
Published 27 April 2007
Online at stacks.iop.org/PMB/52/2775

Abstract

A new imaging technique called emission optical projection tomography (eOPT), essentially an optical version of single-photon emission computed tomography (SPECT), provides molecular specificity, resolution on the order of microns to tens of microns, and large specimen coverage ($\approx$ 1 cubic centimetre). It is ideally suited to gene expression studies in embryos. Reconstructed eOPT images suffer from blurring that worsens as the distance from the axis of rotation increases. This blur is caused in part by the defocusing of the lens' point-spread function, which increases with object distance from the focal plane. In this paper, we describe a frequency space filter based on the frequency–distance relationship of sinograms to deconvolve the distance-dependent point-spread function and exclude highly defocused data from the eOPT sinograms prior to reconstruction. The method is shown to reduce the volume at half-maximum of the reconstructed point-spread function to approximately 20% the original, and the volume at 10% maximum to approximately 6% the original. As an illustration, the visibility of fine details in the vasculature of a 9.5 day old mouse embryo is dramatically improved.

1. Introduction

Rapid advances in genetic research using animal models have driven the demand for three-dimensional biological imaging of small specimens. 3D visualization of whole organs or organisms is often used to gain a better understanding of the development of complex anatomy. Information pertaining to the time and location of gene expression throughout a complete organism is also crucial for understanding developmental genetics.

As a result, there is an increased demand on imaging techniques to have large specimen coverage, cellular-level resolution and molecular specificity. Several techniques have been

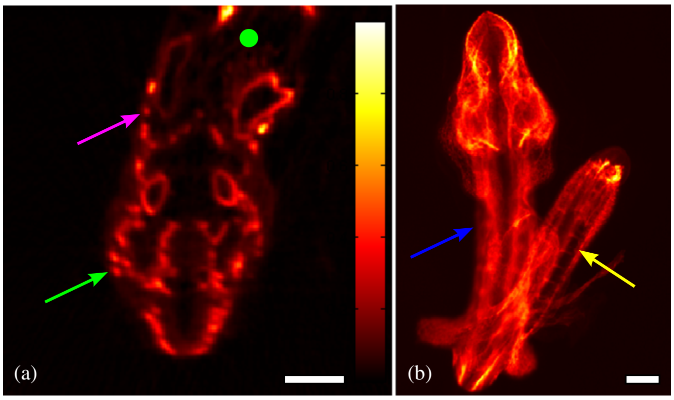

Figure 1. The eOPT reconstruction of vasculature passing through the torso of a mouse embryo (a) is too blurred to distinguish all the different components. Vessels far from the rotational axis (solid green circle) have a greater angular blur (green arrow) than those that are nearer (pink arrow). This blur arises due to eOPT views (b) that contain both in-focus (yellow arrow) and out-of-focus (blue arrow) images. The scale bars represent 200 μm.

developed to achieve this end. Selective plane illumination microscopy (Huisken *et al* 2004) illuminates a specimen with a sheet of excitation light and images the emitted fluorescence with an orthogonal camera-based detection system. This method cannot accommodate absorbing molecular markers commonly used with brightfield microscopy. Other techniques known as block-face or episcopic imaging (Weninger and Mohun 2002) and surface imaging microscopy (Ewald *et al* 2002) embed a sample, image its surface, remove the imaged layer, and continues the process with the newly exposed tissue. However, these methods are time consuming and prevent the use of the sample for further analysis by other means.

A new technique, named optical projection tomography (OPT), (http://genex.hgu.mrc.ac.uk/OPT_Microscopy/optwebsite/introduction/definition/definition.htm.htm) is a relatively new technology that obtains resolution on the order of microns to tens of microns, large specimen coverage (≈ 1 cubic centimetre), and is able to use both absorbing and fluorescent molecular markers (Sharpe *et al* 2002). Use of this technology for biological studies in model organisms (von Both *et al* 2004, Lickert *et al* 2004, Kerwin *et al* 2004 and Tucker *et al* 2004) is increasing.

Reconstructed OPT images suffer from blurring that worsens with increasing distance from the rotational axis, as shown in figure 1(a). This blur is due in part to the collection of images with varying degrees of defocus inherent in optical imaging, as shown in figure 1(b). In any given optical image, the objects at the focal plane are in best focus, the objects within the depth of field (DOF) are considered to be in focus and the objects outside the depth of field are considered to be out of focus.

Specimens in OPT imaging are normally positioned such that half the specimen is positioned within the depth of field, and the other half without, as shown in figure 2. As a result, some out-of-focus data from the half of the specimen outside the depth of field are superimposed on the in-focus data from within the depth of field. This out-of-focus data are included in the filtered back-projection reconstruction process and contribute to the lack of focus in the 3D image.

Other microscopic imaging techniques face similar issues with out-of-focus data. Confocal microscopy (Pawley 1995) attempts to remove as much out-of-focus data as possible by using a pinhole at the detector plane conjugate to the focal plane, so as to exclude as much

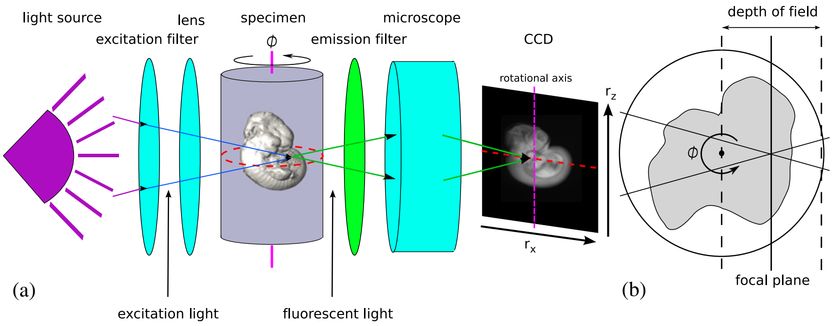

Figure 2. Diagram of optical projection tomography (OPT). (a) Light from a mercury lamp is focused onto the specimen, and fluorescent light emitted from fluorophores is collected by a microscope and recorded by a CCD. The specimen is rotated and views at multiple angles are acquired. (b) The depth of field is positioned over the half of the specimen nearest the lens. The CCD axes are labelled r_x and r_z for detector element and detector row, respectively, and the angle of rotation is labelled ϕ.

(This figure is in colour only in the electronic version)

out-of-focus light as possible. Deconvolution microscopy (McNally *et al* 1999) deals with the out-of-focus data by deconvolving the 3D point-spread function (PSF) of the optical system from a series of images with different positions of the focal plane throughout the specimen.

These techniques are not applicable to OPT. Using a point-sampling technique with OPT would significantly increase imaging time and negate one of its key strengths. Direct deconvolution of the 3D PSF is complicated by the rotation of the object and thus differing projection angles of the OPT views.

In this paper, we describe a method of filtering the frequency space information of 3D OPT sinograms using the frequency–distance relationship (FDR) (Xia *et al* 1995) to exclude the out-of-focus data and to narrow the point-spread function of the in-focus data. The filter is tested with both simulated and real data, and the technique is illustrated using the finely structured fluorescently labelled vasculature of a 9.5 day old mouse embryo.

2. Theory

2.1. Description of optical projection tomography

Since optical projection tomography has been reviewed elsewhere (Sharpe 2004), only a brief description is provided here. A small (≈1 cc) semi-transparent specimen is embedded in agarose and refractive index matched with a 1:2 mixture of benzyl alcohol and benzyl benzoate (BABB). The index-matched specimen is then immersed in a BABB bath with optically flat parallel glass windows. An image of the specimen is formed using an optical microscope as shown in figure 2(a).

OPT images can be created in two different modes: emission OPT (eOPT) and transmission OPT (tOPT). In the case of eOPT, the microscope gathers fluorescent photons emitted from fluorophores throughout the sample that have been excited by wide-field illumination from a mercury vapour arc lamp. The fluorescent photons are separated from the incident illumination by a chromatic filter and focused to an image at the detector. In this paper, we discuss only emission OPT, but will continue to use the OPT acronym. It is expected that this technique will also be applicable in tOPT.

The image formed by the microscope is recorded by a cooled charge coupled device (CCD) camera, in order to minimize noise and increase detection efficiency. The data recorded by a pixel comes from a narrow cone of light, as defined by the lens, that approximates a strip integral projection through the specimen. The axes of all the cones of light collected by the pixels in the CCD frame diverge by less than 0.3° (Sharpe *et al* 2002), and can be approximated as parallel ray projections through the sample. An image at any given rotation angle is termed a view. Each view recorded by the CCD represents the integrated intensity of fluorescence projected along parallel rays through the specimen.

The specimen is rotated stepwise through a complete revolution with views acquired at each step. The rows of the CCD pixels are aligned perpendicularly to the rotational axis. A complete revolution is necessary in order to obtain in-focus data from all parts of the specimen and to allow unambiguous 3D reconstruction. The temporal sequence from a row of detectors forms a sinogram that reconstructs the corresponding slice using a standard convolution filtered back-projection algorithm (Slaney and Kak 1988). A 3D volumetric representation of the specimen is obtained by reconstructing the sinograms from all slices. It should be noted that because all rays are approximately parallel, this reconstruction does not require a cone beam reconstruction, such as described by Feldkamp *et al* (1984).

In all OPT views, there is a limited region in the object, defined by the depth of field, over which the specimen is in acceptable focus. Any part of the specimen positioned outside the depth of field at a given view angle is out of focus in that recorded view. In OPT, the focal plane is positioned such that it is approximately 1/2 the way between the nearest point of the specimen and the rotation axis. Thus, each OPT view consists of both the in-focus data from the proximal half of the specimen and the out-of-focus data from the distal half of the specimen (figure 2(b)).

The OPT technique is similar to optical computed tomography (optical-CT) (Doran *et al* 2001, Doran and Krstajić 2006, Oldham *et al* 2001, Wolodzko *et al* 1999), which has been explored in the field of 3D dosimetry in radiation therapy, but differs by, among other things, the use of image forming optics to create projections through the sample.

2.2. *Trade-off between resolution and depth of field*

The resolution of an optical system is the minimum distance of separation necessary between two point objects such that their images can still be resolved according to the Rayleigh criterion (Pawley 1995). This distance is limited by the 2D point-spread function (PSF) at the focal plane of the optical system, that is, the Airy diffraction pattern, for which the radius r_{Airy} of the first dark ring is given by the equation

$$r_{\text{Airy}} = \frac{0.61 n\lambda}{\text{NA}}, \tag{1}$$

where n is the refractive index of the immersion medium of the lens (in this case $n \sim 1$ for air), λ is the wavelength of light and NA is the numerical aperture of the optical system. The 2D PSF of the optical system is the cross section of the 3D PSF of the optical system, and varies according to the distance between the object and the focal plane. As a result, this resolution r_{Airy} applies only at the focal plane of the optical system. Away from the focal plane, the resolution deteriorates. The optical system has a bandlimit frequency beyond which there is no spatial frequency information. This bandlimit is proportional to the NA of the optical system and is fixed regardless of the degree of defocus (Born and Wolf 1980).

Objects located within the depth of field (DOF) of the optical system are considered to be in focus, but not at best focus. Beyond the depth of field, objects are out of focus. The DOF is given by (Inoué and Spring 1997)

$$\mathrm{DOF} = n_{\mathrm{bath}}\left(\frac{n\lambda}{\mathrm{NA}^2} + \frac{n}{M\mathrm{NA}}e\right), \qquad (2)$$

where M is the lateral magnification of the imaging system, e is the pixel size of the CCD, and n_{bath} is the refractive index of the medium in which the specimen rests, included to account for the effect of foreshortening along the optical axis.

According to the Nyquist criterion of sampling frequency, the Airy disc must be sampled with a detector spacing less than half this distance in order to avoid aliasing and any associated artefacts (Slaney and Kak 1988). This requires the detector spacing to be

$$e \leqslant M\frac{r_{\mathrm{Airy}}}{2}. \qquad (3)$$

This equation can be substituted into equation (2) to determine the maximum possible depth of field $\mathrm{DOF}_{\mathrm{max}}$ (assuming an air immersion medium $n \sim 1$):

$$\mathrm{DOF}_{\mathrm{max}} = n_{\mathrm{bath}}\left(\frac{1.305\lambda}{\mathrm{NA}^2}\right). \qquad (4)$$

Equations (1) and (4) describe the conventional optics trade-off between obtaining the best resolution with a high NA and maximizing the depth of field with a low NA. The typical OPT arrangement is to choose an NA such that the depth of field is equal to or larger than the maximum specimen extent d_{max}.

The image of a point object positioned at any radius from the rotational axis would then be in focus for half a revolution, and out of focus for the other half. Note that objects positioned at less than half the distance of the DOF from the rotational axis would never be imaged at best focus, and objects positioned beyond that would experience best focus at two positions in one revolution.

As a result, a reconstructed OPT image would use images of the object with varying amounts of defocus due to the varying PSF, and that best focus data would rarely be obtained during a complete revolution.

The defocus in OPT imaging could be lessened by reducing the NA by a factor of $\sqrt{2}$ so that the DOF spans the entire specimen extent d_{max}. While the OPT views acquired would exhibit less defocusing over an entire revolution, the best resolution would deteriorate and the bandlimit frequency of the system would be reduced by the same factor of $\sqrt{2}$. This would ultimately restrict the spatial frequency information that can be recovered through digital processing. Thus the typical OPT arrangement maximizes the spatial frequency bandlimit of the acquired OPT views while retaining a half-revolution of in-focus data, at the cost of acquiring significantly defocused data.

2.3. The frequency–distance relationship

The frequency–distance relationship (FDR) of the sinogram data and its Fourier transform was developed by Xia *et al* for single-photon emitted computed tomography (SPECT) (Xia *et al* 1995), an imaging modality that also suffers from a spatially varying PSF. Glick *et al* applied the FDR to 3D SPECT according to Glick *et al* (1994)

$$P(R_x, R_z, \Phi) = H\left(R_x, R_z, l = -\frac{\Phi}{R_x}\right)^{-1} P_b(R_x, R_z, \Phi), \qquad (5)$$

where (R_x, R_z, Φ) is the Fourier equivalent of the sinogram space (r_x, r_z, ϕ) as shown in figure 2. Specifically, (r_x, r_z) are the axes of detector element (perpendicular to the rotational axis) and detector row (parallel to the rotational axis) respectively, l is slope of the line in the

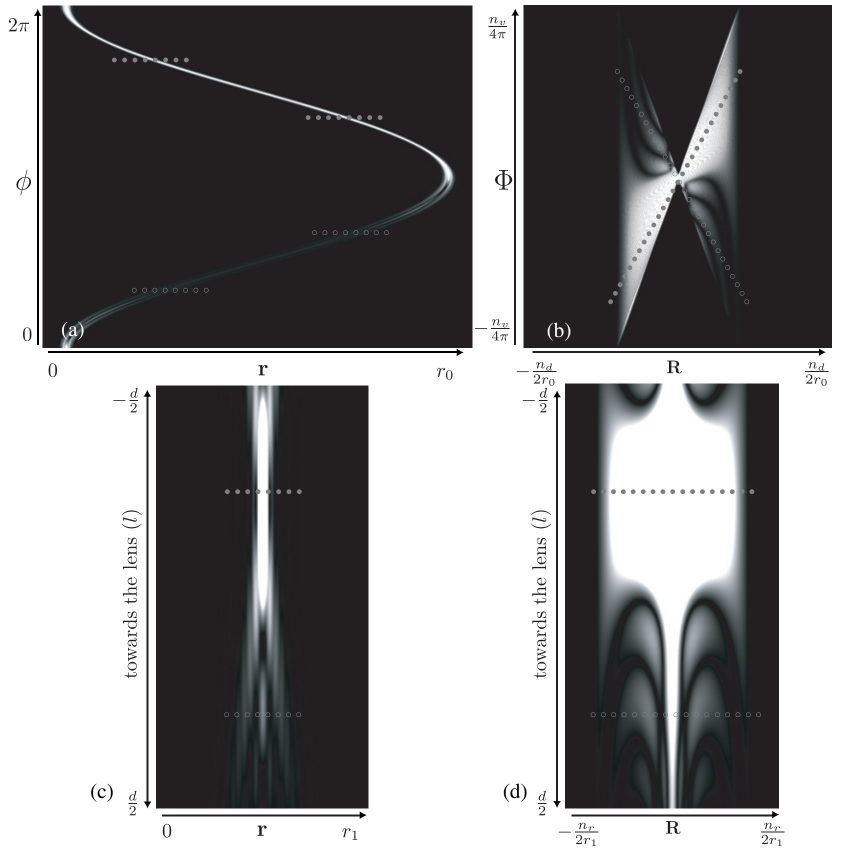

Figure 3. The distance-dependent point-spread function (PSF) in an OPT sinogram of a point object (a) can be separated in Fourier space. The magnitude image of the 2D FT (b) demonstrates a bowtie shape. The PSF recorded at a given view angle is equivalent to the PSF of the lens (c) at a given object-to-lens distance. Similarly, the values of the 1D FT taken transverse to the beam axis (d) of the distance-dependent PSF (c) are approximately equal to the values in the 2D FT along a line of constant slope. In this image, the PSF along the lines • or ○ are approximately equal in both (a) and (c), and similarly in (b) and (d). Images are appropriately windowed for visibility, and the sinogram axes ϕ, r, and sinogram frequency space axes Φ, and R have been labelled appropriately, and n_v is the number of views, n_d is the number of detectors along the CCD row, r_0 is the field of view of the detector row, n_r is the number of detectors across the sampled PSF, r_1 is the distance across the sampled PSF, d is the specimen extent and l is the object-to-lens distance.

(R_x, Φ) plane and also the distance of the object from the lens, $P_b(R_x, R_z, \Phi)$ is the blurred sinogram and $P(R_x, R_z, \Phi)$ is the unblurred sinogram. $H\left(R_x, R_z, l = -\frac{\Phi}{R_x}\right)$ is the FT of the distance-dependent PSF, and is evaluated at each sample (R_x, R_z, Φ) using the FDR.

The FDR was formally derived using a stationary phase approximation (Xia *et al* 1995). Here, we present only a graphical description using the OPT simulation (see methods, section 3).

Figure 3 compares the simulated projection data (a) and its 2D FT (b) to the simulated distance-dependent radial PSF of the lens (c) and its 1D FT taken at each distance from the objective lens (d). In the particular case of a point object, the line with the maximum slope in the 2D FT of the sinogram is approximately equal to the 1D FT of the PSF nearest the objective lens, and the line with the most negative slope is approximately equal to the 1D FT of the PSF furthest from the objective lens. As expected, the lines with slopes in between this maximum and minimum are approximately equal to the corresponding position as denoted by the lines denoted with the symbols • and ○ in (c) and (d). The full range of distance-dependent PSFs is separated along lines of corresponding slopes in the 2D FT of the sinogram. This separation in Fourier space enables the construction of an inverse filter to recover the unblurred sinograms by deconvolving the distance-dependent PSF from the blurred sinograms.

Typical FDR recovery filters used in SPECT are based on a Gaussian PSF whose linewidth increases with distance from the source to the detector. This differs from OPT, which has a complicated bandlimited PSF that varies significantly in frequency space content with increasing distance from the source to the focal plane. In addition, the focal plane is positioned partway through the specimen, rather than best focus being obtained at the point nearest the detector. These differences must be taken into account when constructing an FDR-based recovery filter for OPT.

3. Methods

3.1. OPT simulation

An OPT simulation was used to analyse the reconstruction blur and evaluate the performance of the inverse filter. The simulation calculated the position of a point object at a given rotational angle ϕ, determined the object-to-lens distance and simulated the image of the point by resampling the corresponding 2D lens PSF. This process was repeated for a complete revolution to obtain a full OPT data set. Light attenuation through the sample was not simulated.

The 2D PSF of the optical system was calculated using the XCOSM software package (http://www.essrl.wustl.edu/~preza/xcosm/), and the PSF was assumed to be shift-invariant in the plane orthogonal to the optical axis. Simulations were performed with the optical parameters $\lambda = 535$ nm, NA $= 0.1$, $M = 1.0$, $n = 1.0$ and $n_{\mathrm{bath}} = 1.56$. The resolution at best focus of this simulated system is $r_{\mathrm{Airy}} = 3.26\ \mu$m. The detector spacing in the simulation was set to be $e = 0.1\ \mu$m in order to obtain many pixels across the PSF to aid in evaluating the extent of resolution improvement. According to equation (2), this results in a depth of field DOF $= 86.58\ \mu$m, which is smaller than the maximum depth of field $\mathrm{DOF}_{\mathrm{max}} = 108.9\ \mu$m of the system if the detector sample size was just sufficient to meet the Nyquist sampling criteria, as in equation (4). The principles of the simulation hold for a general optical system of any value of NA.

The radial PSF of the lens was first calculated for a series of point object distances using the XCOSM software package, then resampled to a 2D grid with the same detector spacing as the simulated OPT views. The 2D FFT of the PSFs was calculated in order to obtain the stack of 2D FTs of the 2D PSFs in the coordinate system (R_x, R_z, l) necessary for FDR filter construction as described below.

The FT of the 2D PSF of the lens demonstrates gaps of information at certain frequency values, as shown in figure 3(d). These gaps first appear at the object-to-lens distances located slightly beyond the extent of the wave depth of field (the first term of equation (2)), and become more dominant as the object-to-lens distance is increased. The distance between the gaps on either side of the focus is independent of detector spacing and was determined empirically to be approximately equal to $\mathrm{DOF}_{\mathrm{max}}$. Since the proposed technique is based on the recovery of frequency space information, the maximum specimen extent d_{max} was calculated using the maximum depth of field $\mathrm{DOF}_{\mathrm{max}}$, regardless of detector spacing. As a result, the simulated system is suitable for specimens with a maximum extent $d_{\mathrm{max}} = 2\mathrm{DOF}_{\mathrm{max}} = 217.83\ \mu$m.

The simulated point object was placed 110 μm from the rotational axis, and the focal plane of the simulated lens was placed at a distance of 55.0 μm from the rotational axis, in the direction towards the lens. The simulated detector comprised 2501 detector elements for a total field of view of 250.1 μm, and 2001 views were simulated through a complete revolution about the rotational axis. The parameters for the simulation and the number of detectors and views were chosen to approximate a continuous function for accurate evaluation of the resolution improvement while keeping within reasonable computing demands.

The 2D simulated sinograms were processed according to equation (5) by the 2D frequency space filter described in section 3.3, and reconstructions were performed with a parallel ray filtered back-projection reconstruction software. The voxel size of the reconstruction was equal to the detector element size of the OPT views.

3.2. Phantom construction and specimen preparation

An OPT phantom was created using 4 μm fluorescent silica beads (micromod sicastar-greenF 40-02-403, excitation wavelength = 490 nm, emission wavelength = 535 nm) embedded in agarose and clarified according to typical OPT procedures (Sharpe *et al* 2002). OPT data of the beads were acquired using typical OPT imaging parameters to test the 3D case.

Mouse embryos aged E9.5 were fixed with Dent's fixative and immunostained using a Cy3 PECAM antibody stain to mark the embryo vasculature with a red fluorophore.

3.3. Frequency space filter construction

The complete frequency space filter H_{final}^{-1} designed for use in OPT imaging is a combination of four distinct components, as described in the equation

$$H_{\mathrm{final}}^{-1} = H_{\mathrm{lim}}^{-1} \cdot W_r \cdot W_W \cdot W_b, \tag{6}$$

where H_{lim}^{-1} is a max-limited recovery filter designed according to the FDR, W_r is a slope-based roll-off filter to exclude out-of-focus data, W_W is a Wiener filter to de-emphasize noise and W_b is a bandlimiting roll-off filter for high frequencies. Each component is described in detail below.

3.3.1. FDR-based recovery filter. The FDR recovery filter H^{-1} is constructed as follows:

(a) Calculate the 3D PSF of the lens.
(b) Calculate the 2D FT of the 2D cross sections of the 3D PSF along the optical axis to create a stack of 2D data with the coordinate system (R_x, R_z, l).
(c) At each position (R_x, R_z, Φ) in H, take the corresponding value from the FTs in (R_x, R_z, l) using the relation $l = -\Phi/R_x$.
(d) Invert H to obtain the recovery filter H^{-1}.

As noted in section 3.1, gaps in the frequency space content first appear at object-to-lens distances located just beyond the wave depth of field. The recovery filter will strongly emphasize these regions of the sinogram FT, and as a result emphasize noise from the acquired data.

To avoid the overemphasis of noise in these information gaps, the vectors in the FDR recovery filter are scaled by a weighting factor according to

$$|H_{\mathrm{lim}}^{-1}| = \begin{cases} |H^{-1}| & : \ |H^{-1}| \leqslant C_t \\ C_t + C_r\left(1 - \exp\left[-\dfrac{|H^{-1}| - (C_t)}{C_r}\right]\right) & : \ |H^{-1}| > C_t, \end{cases} \tag{7}$$

where $|H^{-1}|$ is the magnitude value of the inverse filter constructed, $\left|H_{\mathrm{lim}}^{-1}\right|$ is the magnitude value of the limited inverse filter, C_t is the magnitude value at which the transition begins and C_r is the range we wish to use as a transition to the maximum magnitude $C_t + C_r$. The most commonly used values are $C_t = 10^{-3}$ DC and $C_r = 10^{-4}$ DC, where DC is the magnitude of the dc signal. The phase of the limited inverse filter is equal to the phase of the constructed inverse filter, according to

$$\mathrm{phase}\left(H_{\mathrm{lim}}^{-1}\right) = \mathrm{phase}(H^{-1}). \tag{8}$$

3.3.2. Roll-off filter. The FT of the PSF from without the depth of field is dominated by the gaps of information in frequency space described in section 3.1, and even the max-limited FDR recovery filter cannot adequately recover the signal from these noisy regions without allowing noise to dominate the final image. Since only a half-revolution of views is needed to perform the filtered back-projection reconstruction, the out-of-focus data can be safely excluded from the sinogram. This is accomplished by creating a 'roll-off' filter that de-emphasizes the out-of-focus data along lines of decreasing slope according to the following equation:

$$W_r(R_x, R_z, \Phi) = \begin{cases} 1.0 & : \quad l = -\dfrac{\Phi}{R_x} \leqslant 0 \\ \cos^2\left(\dfrac{\pi}{2}\dfrac{|l|}{w}\right) & : \quad w > l > 0 \\ 0.0 & : \quad l > w, \end{cases} \tag{9}$$

where w is a weighting factor from 0.0 to 1.0 chosen according to the amount of de-emphasis desired. The most commonly used value is $w = 0.3$, as was found to adequately exclude the out-of-focus data while minimizing the sharpness of the roll-off.

The roll-off filter has the side effect of creating a weighting function in the reconstructed image space that falls off with the radius of the point from the centre of rotation. The final reconstructed image must be re-scaled to correct for this effect. Reconstructed images from both filtered and unfiltered projections were blurred by a Gaussian function with a linewidth equal to 5% of the field of view, then divided to obtain the scaling factor to be applied to the final reconstructed image.

3.3.3. Wiener filter. Any deconvolution in frequency space data risks overemphasizing noise, especially in the high-frequency region where noise dominates signal. A Wiener filter is commonly used to avoid this problem by de-emphasizing the frequencies that are mostly noise (King *et al* 1983). The Wiener filter W_W can be expressed as

$$W_W(R_x, R_z, \Phi) = \frac{P_s}{P_s + P_n}, \tag{10}$$

where P_s is the power spectrum of the signal and P_n is the power spectrum of the noise. For data with Poisson noise, P_n can safely be assumed to be constant over all frequencies (Goodman and Belsher 1976). P_n can be estimated by averaging the highest frequency components of the recorded data, where no signal is expected. The power spectrum of the signal can be estimated by radially averaging the power spectrum of the acquired data, subtracting the power spectrum of the noise, and resampling the radial average to the 3D grid. Although this method provides an adequate estimation of the power spectrum of the signal, it loses any of the information about the 2D details of the sinogram FT, such as the known bandlimit of the optical system.

3.3.4. Bandlimit filter. The highest frequencies in the FT of the lens' PSF contain the least amount of energy, and the frequencies beyond the bandlimit of the lens contain no energy at all. The inverse filter will strongly emphasize these values, which in the acquired data are dominated by noise. The bandlimit filter is thus included to explicitly de-emphasize those regions that contain no information yet might not be sufficiently de-emphasized by the radial Wiener filter described in equation (10).

These highest frequency values are rolled down to zero from 90% of the bandlimit of the lens to the 100% of the bandlimit, according to the following equation:

$$W_{b_x}(R_x, R_z, \Phi) = \begin{cases} 1.0 & : \quad R_x < 0.90b \\ \cos^2\left(\frac{\pi}{2}\frac{R_x - 0.90b}{0.1b}\right) & : \quad b > R_x > 0.90b \\ 0.0 & : \quad R_x > b, \end{cases} \tag{11}$$

where b is the bandlimit of the lens.

The same weighting W_{b_z} is used in the R_z direction. The final bandwidth roll-off filter is $W_b = W_{bx} W_{bz}$.

3.4. OPT imaging

Actual OPT data were acquired on an OPT device that included a Leica MZFLIII stereomicroscope using a Plan 0.5×, 135 mm working distance objective lens (Leica 10446157), and a 1.0× camera lens with an 80 mm tube length (Leica 1445930). The images were recorded by a 1376 × 1036 pixel (6.45 μm pitch size) Retiga Exi CCD that was thermoelectrically cooled to −40 °C. Specimens imaged with eOPT were illuminated by a 100 W mercury vapour lamp (Leica 10504069) attached to the microscope housing. A Texas Red filter set (Leica 10446365) was used to isolate the fluorescence of the Cy3 signal. The rotational step size was 0.9°, with a total of 400 images acquired in a complete revolution.

OPT views were acquired using a zoom setting of 5×, a total magnification of 2.5× and an NA of 0.0505. These settings result in a lateral resolution of $r_{\mathrm{Airy}} = 7.13$ μm for a wavelength $\lambda = 590$ nm, an effective sampling size of 2.58 μm and a depth of field of DOF = 441 μm. The maximum specimen extent useable in this particular setup is $d_{\max} = 2\mathrm{DOF}_{\max}$. In this case, $\mathrm{DOF}_{\max} = 471$ μm and $d_{\max} = 942$ μm. It should be noted that, as in the simulation, these values would scale with the use of a different NA.

Exposure time for each OPT view of the beads was 3 s, for a total imaging time of 20 min, and exposure time for each OPT view of the mouse embryos was 500 ms, for a total imaging time of 3.5 min.

Acquired OPT views were processed according to equation (5) by the frequency space filter described in section 3.3 using an experimentally acquired PSF from the silica bead phantom. Reconstructions were performed with parallel ray filtered back-projection reconstruction software. The voxel size of the reconstruction was equal to the detector element size of the OPT views.

3.5. Image evaluation

All reconstructed images were inspected visually to evaluate the differences between the original reconstruction and the reconstruction of the filtered sinograms. For the simulated point objects and beads, a line was plotted through the radial, tangential and z-coordinate axes centred on the beads. The full width at half-maximum (FWHM) and full width at 10% maximum (FW10M) were measured in order to compare the filtered results to the unfiltered results.

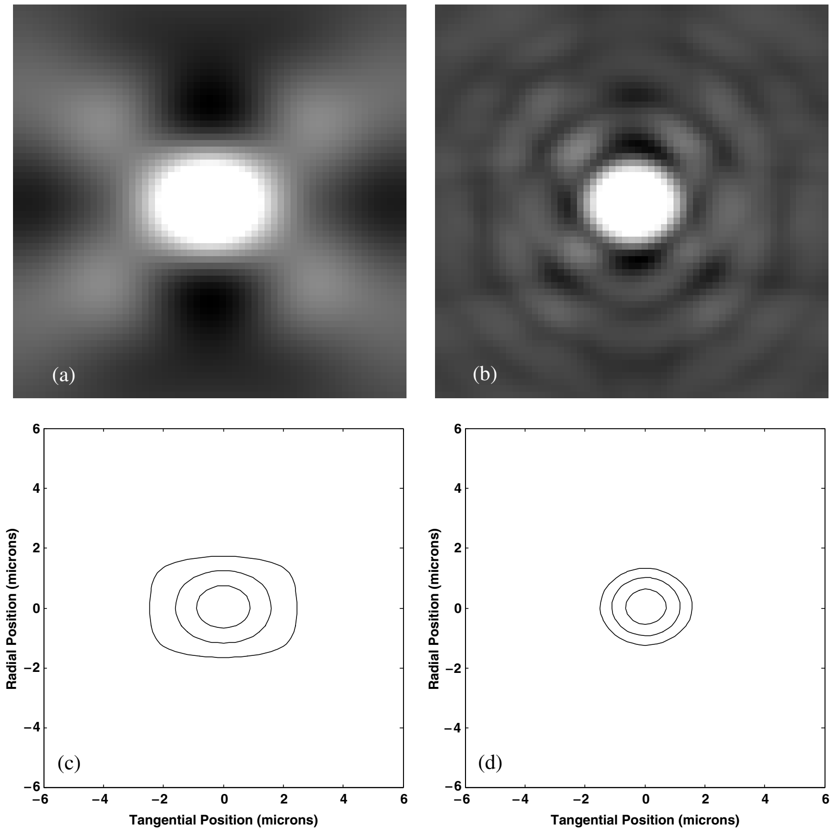

Figure 4. The reconstruction of a point object (a) demonstrates blurring, which is lessened in the filtered reconstruction (b). The contour plots (c) and (d) show the contours of the reconstruction at 20%, 50% and 80% the maximum value.

4. Results and discussion

The reconstruction of the 2D simulation of typical OPT is shown in figure 4 as images and as a contour plot. The reconstructed PSF exhibits a broader tangential than radial spread, as listed in the FWHM and FW10M measurements in table 1. The four lobes positioned around the reconstructed PSF cause additional blur not represented by the measurements. Plots through the radial and tangential axes of the sum-normalized reconstructed images are shown in figure 5. The reconstructed PSF has visibly narrowed, and symmetry has remained about the same at 1:1.3 tangential:radial for the FWHMs, but has improved from 1:1.6 to 1:1.2 at the FW10M. Although some ringing has appeared and some intensity values drop below zero, it is less detrimental to the image than the lobes evident in the unfiltered reconstruction.

The typical reconstruction of the silica bead is contour plotted in figures 6(a)–(c), and the filtered reconstruction is contour plotted in figures 6(d)–(f). The measurements of the FWHM and FW10M reveal improvement along all the three axes, as listed in table 2. The radial and tangential measurements have improved to ∼35–55% and ∼40–60% of the original measurement, respectively. The axial measurement, which was not measurable in the 2D scenario, shows improvement by ∼35–55%. The volume of the reconstructed

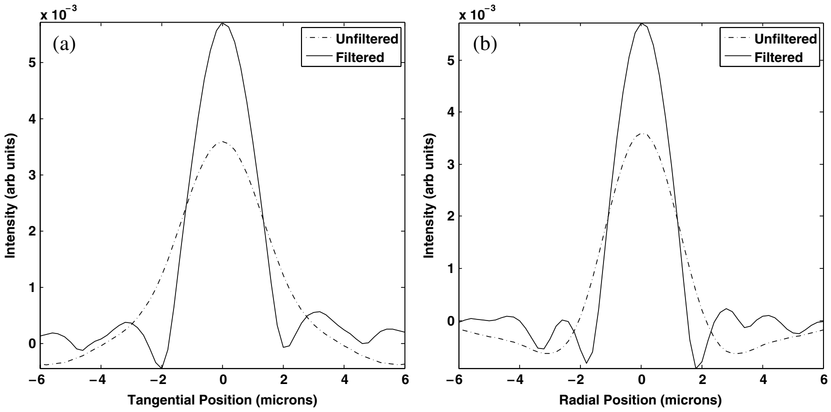

Figure 5. Plots through the radial (a) and the tangential (b) axes of the unfiltered (— · —) and filtered (——) reconstructions in figures 4(a) and (b) demonstrate the general spread of the reconstructed image. The plots of the filtered reconstruction demonstrate a reduced broadening and therefore a higher resolution. The measured values of the FWHM and FW10M are listed in table 1.

Table 1. The FWHM and FW10M of the unfiltered and filtered reconstructions shown in figure 4 and plotted in figure 5.

Direction	FWHM (μm)	FW10M (μm)
Unfiltered radial	1.23 (100%)	1.87 (100%)
Unfiltered tangential	1.61 (100%)	3.07 (100%)
Filtered radial	0.94 (76.4%)	1.38 (74.0%)
Filtered tangential	1.18 (73.6%)	1.72 (55.9%)

Table 2. The FWHM and FW10M of the unfiltered and filtered reconstructions shown in figure 6.

Direction	FWHM (μm)	FW10M (μm)
Unfiltered radial	18.8 (100%)	40.6 (100%)
Unfiltered tangential	15.7 (100%)	35.0 (100%)
Unfiltered axial	15.7 (100%)	35.0 (100%)
Filtered radial	11.6 (61.7%)	17.5 (43.1%)
Filtered tangential	8.7 (55.4%)	12.8 (36.6%)
Filtered axial	8.4 (53.5%)	13.0 (37.1%)

PSF at half-maximum is 18.9% the original, and the volume at 10% maximum is 5.9% the original measurement. Symmetry has improved notably. Brightness is conserved over the reconstructed image.

It is noted again that this test scenario applies only to a point on the periphery of the imaged specimen. The distance-dependent PSF of the lens results in a radially dependent reconstructed PSF, each of which would undergo different degrees of improvement. The object on the periphery is studied as it is expected to undergo the most defocusing and hence would result in the most blurred reconstruction.

The biological sample was imaged to test not only the effects on a fine detailed structure, but also to evaluate the performance of the filter across all radii from the rotational axis. The resolution improvement can be seen directly in the OPT projections or views of the mouse

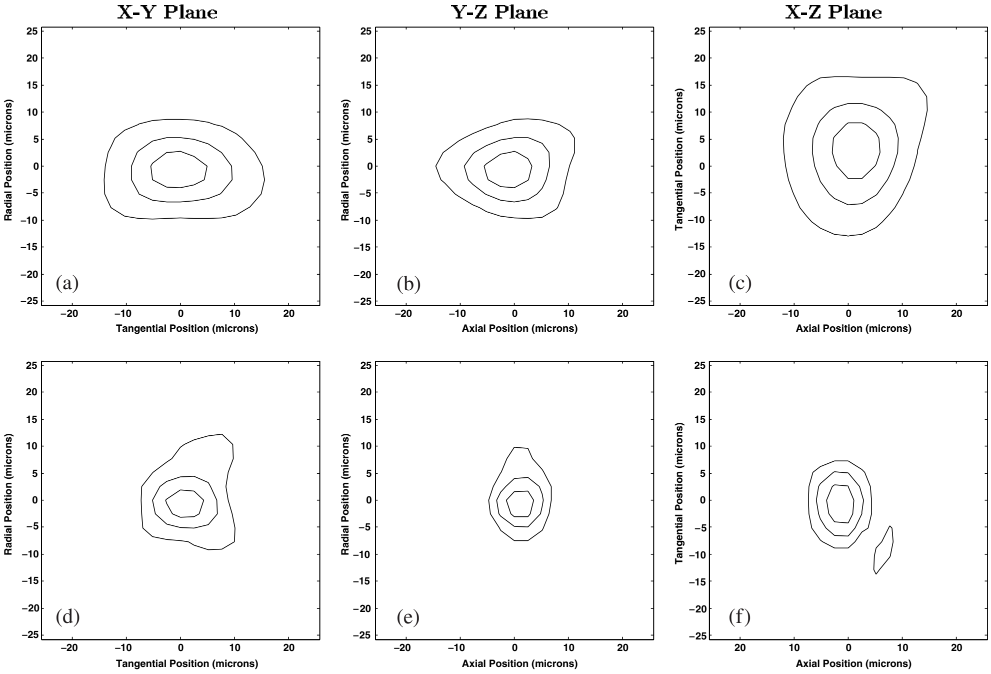

Figure 6. Contour plots of the three planes (a)–(c) in an OPT reconstruction of a subresolution bead demonstrate broadening that is significantly lessened in the reconstruction of the filtered sinograms shown in (d)–(f). The contour lines are drawn at 20%, 50% and 80% the maximum value. The FWHM and FW10M of the plots are listed in table 2.

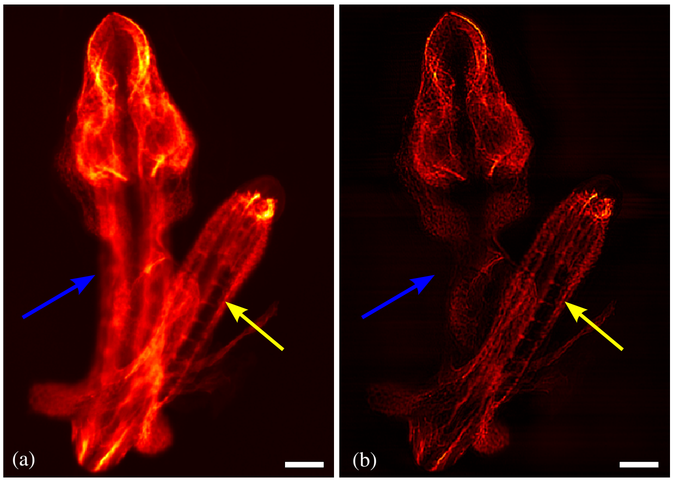

Figure 7. Images of objects that are out-of-focus (blue arrow) in the original eOPT projection (a) have been removed in the filtered eOPT projection (b) prior to reconstruction. Images of objects that are in-focus (yellow arrow) have been generally sharpened. The scale bars represent 200 μm.

embryo vasculature, as in figure 7. The in-focus portion of the view has been generally sharpened, and the out-of-focus portion of the data has been removed.

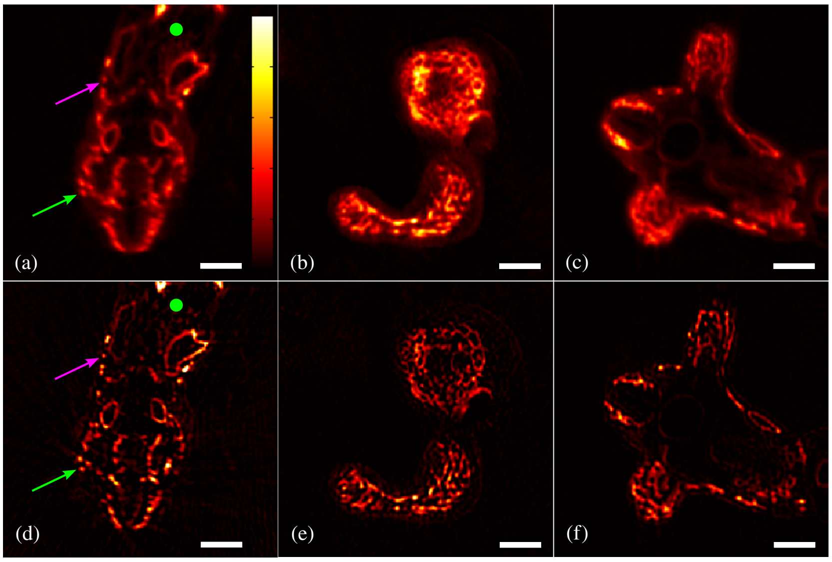

Figure 8. The resolution improvement is most notable in the reconstructions of the 3D biological sample. The mouse vasculature shown in figure 1 is replicated in (a), along with two orthogonal planes through the mouse cardiac system and tail (b) and through the tail and limb buds (c). The corresponding reconstructions from the filtered sinograms (d)–(f) show marked improvement in resolving the individual vessels and decreasing overall blur. The angular blur (green arrow) evident in vessels far from the rotational axis (green circle) has been reduced, and is now comparable in shape to the vessel near the rotational axis (pink arrow). The colour bar in (a) is the colour map for all images, with a display range from 0.0 to the maximum image value, except (d) which has a display range of 0.0–0.5 the maximum image value. The scale bars represent 200 μm.

The resolution improvement is most notable in the reconstructed images of the mouse embryo vasculature. In the initial OPT reconstruction of the mouse embryonic vasculature, as shown in figure 8(a), the vessels near the rotational axis were visible and recognizable, but the vessels near the exterior were unrecognizable as blur dominates the image. Filtering the data has improved not only the vessels near the periphery, as shown in figure 8(d), but also the vessels near the rotational axis as well. Orthogonal image planes of the original reconstruction (shown in figures 8(b), (c)) and the filtered reconstruction (8(e), (f)) exhibit similar improvement along the axial direction.

5. Conclusion

We have demonstrated the use of a frequency space filter based on the frequency–distance relationship to improve the resolution of reconstructed emission OPT images. This filter de-emphasizes and excludes the out-of-focus data obtained from objects outside the depth of field, de-emphasizes frequency components that are dominated by noise and deconvolves the distance-dependent point-spread function from images of objects within the depth of field. OPT reconstructions of simulated point objects demonstrate reconstruction point-spread functions with reduced FWHM and FW10M in all axes, with a notable improvement in symmetry. Though some ringing is evident, it minimally degrades the reconstructed image. The advantages of the inverse filter are most notable when applied to the experimental OPT data. The use of the inverse filter described in this paper allows much greater biological clarity as seen in the reconstructions of vasculature in an E9.5 mouse embryo.

The filter can be further refined by implementing a non-negativity constraint in an iterative filtering process to prevent the introduction of negative intensity value artefacts. The filtering technique is also expected to provide similar improvements to transmission OPT data in future work.

Acknowledgments

The research in this paper has been funded by the Canadian Foundation for Innovation and the Ontario Research and Development Challenge Fund. We would like to thank the British Medical Research Council for providing us with an OPT device. We also thank the Janet Rossant lab for providing specimens for study. We appreciate the insightful comments about the paper from Jim Swoger in the Sharpe lab. RMH holds a Canada Research Chair in Imaging, and JRW is funded with an Ontario Graduate Scholarship.

References

Born M and Wolf E 1980 *Principles of Optics* 6th edn (Oxford: Pergamon)

Doran S J, Koerkamp K K, Bero M A, Jenneson P, Morton E J and Gilboy W B 2001 A CCD-based optical scanner for high-resolution 3D imaging of radiation dose distributions: equipment specifications, optical simulations and preliminary results *Phys. Med. Biol.* **46** 3191–213

Doran S J and Krstajić N 2006 Focusing optics of a parallel beam CCD optical tomography apparatus for 3D radiation gel dosimetry *Phys. Med. Biol.* **51** 2055–75

Ewald A J, McBride H, Reddington M, Fraser S E and Kerschmann R 2002 Surface imaging microscopy, an automated method for visualizing whole embryo samples in three dimensions at high resolution *Dev. Dyn.* **225** 369–75

Feldkamp L A, Davis L C and Kress J W 1984 Practical cone-beam algorithm *J. Opt. Soc. Am.* **1** 612–9

Flannery B P, Deckman H W, Roberge W G and D'Amico K L 1987 Three-dimensional x-ray microtomography *Science* **237** 1439–44

Foster F S, Pavlin C J, Harasiwicz K A and Christopher D A 2000 Advances in ultrasound biomicroscopy *J. Ultrasound Med. Biol.* **26** 1–27

Glick S J, Penney B C, King M A and Byrne C L 1994 Noniterative compensation for the distance-dependent detector response and photon attenuation in SPECT imaging *IEEE Trans. Med. Imaging* **13** 363–74

Goodman J W and Belsher J F 1976 Fundamental limitations in linear invariant restoration of atmospherically degraded images *Proc. SPIE* **75** 141–54

Hecksher-Sørensen J and Sharpe J 2001 3D confocal reconstruction of gene expression in mouse *Mech. Dev.* **100** 59–63

Huisken J, Swoger J, Del Bene F, Wittbrodt J and Stelzer E H K 2004 Optical sectioning deep inside live embryos by selective plane illumination microscope *Science* **305** 1007–9

Inoué S and Spring K R 1997 *Video Microscopy* 2nd edn (New York: Plenum)

Johnson G A, Cofer G P, Gewalt S L and Hedlund L W 2002 Morphologic phenotyping with MR microscopy: the visible mouse *Radiology* **222** 789–93

Jorgensen S M, Demirkaya O and Ritman E L 1998 Three-dimensional imaging of vasculature and parenchyma in intact rodent organs with x-ray micro-CT *Am. J. Phys.* **275** H1103–14

Kerwin J *et al* 2004 3 dimensional modelling of early human brain development using optical projection tomography *BMC Neurol.* **5** 27

King M A, Doherty P W and Schwinger R B 1983 A Wiener filter for nuclear medicine images *Med. Phys.* **10** 876–80

Lickert H, Takeuchi J K, von Both I, Walls J R, McAuliffe F, Adamson S L, Henkelman R M, Wrana J L, Rossant J and Bruneau B G 2004 Baf60c is essential for function of BAF chromatin remodelling complexes in heart development *Nature* **431** 107–12

McNally J G, Karpova T, Cooper J and Conchello J A 1999 Three-dimensional imaging by deconvolution microscopy *Methods* **19** 373–85

Oldham M, Siewerdsen J H, Shetty A and Jaffray D A 2001 High resolution gel-dosimetry by optical-CT and MR scanning *Med. Phys.* **28** 1436–45

Pawley J (ed) 1995 *Handbook of Biological Confocal Microscopy* 2nd edn (New York: Plenum)

Potter S M, Fraser S E and Pine J 1996 The greatly reduced photodamage of 2-photon microscopy enables extended 3-dimensional time lapse imaging of living neurons *Scanning* **18** 147

Sharpe J, Ahlgren U, Perry P, Hill B, Ross A, Hecksher-Sørensen, Baldock R and Davidson D 2002 Optical projection tomography as a tool for 3D microscopy and gene expression studies *Science* **296** 541–5

Sharpe J 2004 Optical projection tomography *Annu. Rev. Biomed. Eng.* **6** 209–24

Slaney M and Kak A C 1988 *Principles of Computerized Tomographic Imaging* (New York: IEEE)

Tucker A S, Watson R P, Lettice L A, Yamada G and Hill R E 2004 Bapx1 regulates patterning in the middle ear: altered regulatory role in the transition from the proximal jaw during vertebrate evolution *Development* **131** 1235–45

von Both I, Silvestri C, Erdemir T, Lickert H, Walls J R, Henkelman R M, Rossant J, Harvey R P, Attisano L and Wrana J L 2004 Foxh1 is essential for development of the anterior heart field *Dev. Cell* **7** 331–45

Weninger W J and Mohun T 2002 Phenotyping transgenic embryos: a rapid 3-D screening method based on episcopic fluorescence image capturing *Nat. Genet.* **30** 59–65

Wolodzko J G, Marsden C and Appleby A 1999 CCD imaging for optical tomography of gel radiation dosimeters *Med. Phys.* **26** 2508–13

Xia W, Lewitt R M and Edholm P R 1995 Fourier correction for spatially variant collimator blurring in SPECT *IEEE Trans. Med. Imaging* **14** 100–15